Ocean Modelling 94 (2015) 1–14

Contents lists available at ScienceDirect

Ocean Modelling

journal homepage: www.elsevier.com/locate/ocemod

Multi-layer quasi-geostrophic ocean dynamics in Eddy-resolving regimes

I.V. Shevchenko*, P.S. Berloff

Department of Mathematics, Imperial College London, Huxley Building, 180 Queen's Gate, London SW7 2AZ, UK

ARTICLE INFO

Article history:
Received 19 February 2015
Revised 22 July 2015
Accepted 31 July 2015
Available online 7 August 2015

Keywords:
Multi-layer quasi-geostrophic model
Eddy resolving simulations
Long-time runs
Large Reynolds number
Nonlinear eddy dynamics
High baroclinic modes

ABSTRACT

The multi-layer quasi-geostrophic model of the wind-driven ocean gyres is numerically investigated using a combination of long-time runs (200 years) needed for accurate statistics, spatial resolutions (grid interval of less than one kilometer) needed for accurate representation of mesoscale eddies, and large Reynolds number ($Re > 10^4$) needed for more realistic flow regimes. We gradually increased the Reynolds number by lowering the eddy viscosity and analysed the corresponding changes of the large-scale circulation, energetics and eddy fluxes, with the goal to understand how the nonlinear eddy dynamics affects the large-scale ocean circulation, as more and more degrees of freedom become dynamically available. Three- and six-layer configurations of the model are considered in order to understand effects of higher baroclinic modes. A parameter sensitivity study is also carried out to show that the explored flow regime is robust.

As *Re* increases, most properties of the flow show no signs of approaching an asymptote, and the following tendencies are found. The time-mean flow properties tend to an asymptote in the three-layer model but not in the six-layer one, suggesting that higher baroclinic modes are dynamically more active at larger *Re*. The eddy kinetic and potential energies grow faster in the six-layer case. The intensity of the eddy forcing (eddy flux divergence) increases with *Re*. The inter-gyre eddy potential vorticity flux is predominantly northward and up-gradient for all *Re* studied. A comparison of the three- and six-layer model solutions revealed an inhibitory influence of high baroclinic modes on the penetration length of the eastward jet extension of the western boundary currents and on the strength of the adjacent recirculation zones. In large-*Re* regimes, the population of eddies is mostly sustained by the eddy generation at the eastern end of the eastward jet rather than in its central section. Finally, by studying the numerical convergence of the solutions, we found the empirical dependency between the eddy viscosity and the required grid resolution: halving the viscosity requires halving the grid spacing.

1. Introduction

The ocean is one of the largest and least understood components of the global climate system. Being a player of fundamental importance in climate variability, the ocean still anchors the accuracy of climate models. One of the limiting factors is our inability to resolve oceanic submesoscale eddies characterised by the length scale $O(1)$ km. For the time being, there are neither experimental facilities nor mathematical models of the ocean that could provide geoscientists with high-resolution and long-time data coverage permitting to study how different multiscale flow components interact. Whereas detailed global ocean measurements on all scales are out of the question for a long time to come, the leading-edge results in numerical modelling instill confidence that high-resolution eddy simulations may become feasible in the near future. Recently, ocean general circulation models (OGCMs) based on nested grids and operating at high resolutions started to appear (Gula et al., 2015). However, such a possibility is not yet within the reach of the modern OGCMs operating on the planetary scale due to their incapability to operate in fully Eddy-resolving regimes, that is, with resolved scales down to 1 km. Even with the cutting-edge model resolution of 1/12°, the eddies are still only marginally resolved and the simulation times are only tens of years (Marsh et al., 2009; Treguier et al., 2014). Although recent milestone simulations, used the MIT general circulation model, demonstrate the ability of the model to work at very high spatial resolutions (1/146° to 1/50° horizontal grid spacing and 90 vertical levels) and to resolve the eddies (Armstrong et al., 2014), the simulation times are short and systematic exploration of the solution convergence and parameter sensitivity studies are unfeasible (Armstrong et al., 2014). However, yet the lack of immense computational power corners OGCMs into unavoidable eddy parameterisation which, being so far largely inaccurate, remain an Achilles heel of the ocean modelling. This sets a favourable situation for lighter oceanic models to guide the research of ocean eddy dynamics until OGCMs can resolve all important length scales for long-time runs.

* Corresponding author. Tel.: +447935872407.
E-mail address: i.shevchenko@imperial.ac.uk (I.V. Shevchenko).

http://dx.doi.org/10.1016/j.ocemod.2015.07.018
1463-5003/

In this work we take this opportunity and consider dynamically viable and featurely enriched quasi-geostrophic (QG) model, which simulates the mesoscale motions well beyond its formal limits of applicability (Mundt et al., 1997; Zurita-Gotor and Vallis, 2009). Our goal and the novelty of this work is to explore the eddy effects for a broad range of Reynolds numbers *Re* so that the flow is increasingly controlled by the explicit nonlinear eddy dynamics rather than by diffusive eddy parameterisation. The other goal is to establish a set of benchmark double-gyre solutions and put forward a methodology for systematic analyses of eddy effects in more advanced, but also much more computationally expensive, primitive-equation ocean models.

There are three precursors to this work. The first one is the work by Holland (1978), who pioneered a two-layer eddy-permitting QG model with the horizontal grid resolution of $dx = 20$ km and showed that dynamically resolved fluctuations feed back on the ocean gyres. The second work is by Barnier et al. (1991) who studied the three- and six-layer double-gyre QG model with the horizontal grid resolution of $dx = 10$ km. The main conclusion of the authors is that the high baroclinic modes play a catalytic role in eddy/mean interactions and, thus, elongate the eastward-jet extensions of the western boundary currents such as the Gulf stream and Kuroshio. The third study is the one by Siegel et al. (2001), in which a benchmark six-layer QG solution of ocean gyres with relatively large *Re* was spun up for six years and run for another three years with the horizontal resolution of $dx = 1.6$ km. The authors concluded that at large *Re* the time-mean kinetic energy is relatively independent of *Re*, but meridional eddy fluxes keep increasing with it. There are also some works studying QG surface dynamics requiring high horizontal and vertical resolutions (e.g. Roullet et al. (2012)), but this dynamics is beyond the scope of our study, where we centre on vertical scales of motion related to the pycnocline and captured by the low baroclinic modes, since these motions are the most important ones for the Gulf stream mesoscale eddy dynamics, which is the main focus of our work.

In our work we continue and extend the past studies by (i) considering much more realistic flow regimes, (ii) reaching much larger *Re*, (iii) refining the horizontal grid resolution down to $dx = 937$ m for more accurate representation of mesoscale eddies, and (iv) by significantly extending the simulation times for much more reliable statistics. Our use of the advanced numerics yields another gaining factor of 4 in terms of the finer spatial resolution (Karabasov et al., 2009), though this factor may be smaller at extremely high resolutions. To summarize, in terms of the dynamically resolved degrees of freedom and achieved simulation years, our benchmark solution is at least 1.5×10^6, 8500, and 500 times more expensive, in terms of the degrees of freedom and simulation time, than the ones in (Holland, 1978), (Barnier et al., 1991), and (Siegel et al., 2001), respectively. We also looked more thoroughly into the time-mean flow and eddy properties and their dependencies on *Re* and studied the dynamic effects of high baroclinic modes.

2. Double-gyre *M*odel

We consider the classical double-gyre QG model, describing idealised midlatitude ocean circulation, in three- and six-layer configurations (denoted as 3L and 6L). The multi-layer QG equations (Pedlosky, 1987; Vallis, 2006) for the potential vorticity (PV) anomaly q in a domain Ω are

$$\partial_t q_i + J(\psi_i, q_i + \beta y) = \delta_{1i} F_{\rm w} - \delta_{iN}\, \mu \Delta \psi_i + \nu \Delta^2 \psi_i, \quad i = 1, 2, \dots, N, \tag{1}$$

where $J(f, g) \equiv f_x g_y - f_y g_x$, and δ_{ij} is the Kronecker symbol; $N = \{3, 6\}$ is the number of stacked isopycnal fluid layers for the 3L and 6L setups with depths (from top to bottom): $H_1 = 0.25$ km, $H_2 = 0.75$ km, $H_3 = 3.0$ km; and $H_1 = H_2 = H_3 = H_4 = 0.25$ km, $H_5 = 1.0$ km, $H_6 = 2.0$ km, respectively. The computational domain Ω is a square, closed, flat-bottom basin of dimensions $L \times L \times 4$ km, with $L = 3840$ km. The asymmetric wind curl forcing (Ekman pumping) drives the double-gyre ocean circulation, and it is given by

$$F_{\rm w} = \begin{cases} -1.80\, \pi\, \tau_0 \sin(\pi y / y_0), & y \in [0, y_0), \\ 2.22\, \pi\, \tau_0 \sin(\pi (y - y_0)/(L - y_0)), & y \in [y_0, L], \end{cases}$$

with a wind stress $\tau_0 = 0.3\,\mathrm{N\,m^{-2}}$ and the tilted zero forcing line $y_0 = 0.4L + 0.2x,\ x \in [0, L]$. Notice that τ is chosen so that to avoid unrealistically strong eastward jet in low-viscosity (high Reynolds number) regimes. The planetary vorticity gradient is $\beta = 2 \times 10^{-11}\,\mathrm{m^{-1}\,s^{-1}}$, the bottom friction parameter is $\mu = 4 \times 10^{-8}\,\mathrm{s^{-1}}$, and the lateral eddy viscosity ν is a variable parameter specified further below.

The layerwise PV anomaly q_i and the velocity streamfunction ψ_i are dynamically coupled through the system of elliptic equations:

$$q_i = \Delta \psi_i - (1 - \delta_{i1}) S_{i1} (\psi_i - \psi_{i-1}) - (1 - \delta_{iN}) S_{i2} (\psi_i - \psi_{i+1}), \quad i = 1, 2, \dots, N, \tag{2}$$

with the stratification parameters S_{i1}, S_{i2} chosen so that the first and the second Rossby deformation radii for the 3L and 6L configurations are $Rd_1 = 40$ km, $Rd_2 = 23$ km; and $Rd_1 = 40$ km, $Rd_2 = 16$ km, $Rd_3 = 11.6$ km, $Rd_4 = 9.8$ km, $Rd_5 = 7.8$ km, respectively. Note that Rd_1 is the same in both configurations as well as H_1. Systems (1 and 2) are augmented with the integral mass conservation constraints (McWilliams, 1977):

$$\partial_t \iint_{\Omega} (\psi_i - \psi_{i+1})\, dy dx = 0, \quad i = 1, 2, \dots, N - 1, \tag{3}$$

with the zero initial condition, and with the partial-slip lateral boundary condition:

$$\partial_{\mathbf{nn}} \psi_i - \alpha^{-1} \partial_{\mathbf{n}} \psi_i = 0, \quad i = 1, 2, \dots, N, \tag{4}$$

where $\alpha = 120$ km and $\mathbf{n}$ is the normal-to-wall unit vector.

The QG model (1–4) is solved with the high-resolution CABARET method based on a second-order, non-dissipative and low-dispersive, conservative advection scheme (Karabasov et al., 2009). The distinctive feature of this method is its ability to simulate large-*Re* flow regimes at much lower, compared to conventional methods, computational costs. An efficient parallelisation of the QG model allowed us to carry out high-performance computations on uniform horizontal grids of size $G = \{129^2, 257^2, 513^2, 1025^2, 2049^2, 4097^2\}$, where the grid of size $X \times X$ is abbreviated as X^2.

Our horizontal grid resolution is consistent with the vertical one so that the shortest deformation radius is at least marginally resolved with 5–10 grid points. Further simultaneous refinement of the horizontal and vertical resolutions is, of course, desirable, but remains beyond the scape of this paper due to the limit of our computational resources.

Finally, we would like to remind that QG approximation relies on several assumptions, and some of them (smallness of the vertical velocity and density anomalies) including the key one - smallness of the Rossby number - break down for submesoscale motions operating on the scales shorter than the relevant Rossby deformation radius. Given our finest nominal grid resolution of about one km and the fact that numerical schemes typically require 5–10 grid points to represent a length scale with reasonable accuracy (Karabasov et al., 2009), we model the length scales down to 5–10 km, which may be near the edge of formal QG applicability.

3. Analyses of the double-gyre solutions

In this section we describe various properties of the ocean model solutions, study main dependencies of the large-scale flow and mesoscale eddies on the Reynolds number *Re* and define some diagnostics for the next sections. The total basin-average time-mean potential $\overline{P}$ and kinetic $\overline{K}_i$ energies of the flow are given by

$$\overline{P} = \frac{1}{2}\sum_{i=1}^{N-1}\frac{H_i S_{i2}}{A}\iint_{\Omega}\overline{(\psi_i-\psi_{i-1})^2}\,dydx\,,\quad i=2,3,\ldots,N\,,$$

$$\overline{K}_i = \frac{1}{2}\frac{H_i}{A}\iint_{\Omega}\overline{(\nabla\psi_i)^2}\,dydx\,,\quad i=1,2,\ldots,N,$$

where $A = L_xL_yH$, and $H = \sum_{i=1}^{N} H_i$. By decomposing $\psi_i = \overline{\psi}_i + \psi_i'$ into the time-mean (overbared) and fluctuating (primed) components, we define the eddy potential energy $\overline{EPE}$ and the eddy kinetic energy $\overline{EKE}_i$ as

$$\overline{EPE} = \frac{1}{2}\sum_{i=1}^{N-1}\frac{H_i S_{i2}}{A}\iint_{\Omega}\overline{(\psi_{qi}'-\psi_{i-1}')^2}\,dydx\,,\quad i=2,3,\ldots,N,$$

$$\overline{EKE}_i = \frac{1}{2}\frac{H_i}{A}\iint_{\Omega}\overline{(\nabla\psi_i')^2}\,dydx\,,\quad i=1,2,\ldots,N,$$

and the energies of the mean flow, denoted by angular brackets, are found as

$$\langle P\rangle = \overline{P}-\overline{EPE},\quad \langle K\rangle_i = \overline{K}_i-\overline{EKE}_i\,,\quad i=1,2,\ldots,N.$$

We also introduce the eddy PV flux divergence $J_i' = -(J(\psi,q)-J(\overline{\psi},\overline{q}))$, referred to as the eddy forcing, its time mean $\overline{J_i'}$ and standard deviation $\sigma\left(-J_i'\right)$, as well as the corresponding time-mean eddy PV flux $\overline{F_i'} = \overline{\mathbf{v}_i'q_i'}$, where $\mathbf{v}_i = (\partial_y\psi_i, -\partial_x\psi_i)$. To compute the upper-layer time-mean eddy PV flux $\overline{F_1'}$ between the gyres, we calculated the integral

$$\overline{F_S'} = \int_S \overline{F_1'}\cdot\mathbf{n}\,dS$$

over the separatrix S - the line with $\min_{\Omega'}(\overline{F_1'})$, where Ω' is a domain that includes the eastward jet and contains the most intensive eddy forcing; $\mathbf{n}$ is the unit normal vector pointing northward. The Ω-average integral of a function $f(x, y)$ is denoted by $I_\Omega(f)$, and $\overline{f}_j^{(N),k}$ stands for the time-mean value of f computed on a k^2 grid for the N-layer model on the jth layer.

We define the maximum Reynolds number as

$$Re = \overline{U}Rd_1/\nu,$$

where $\overline{U}$ is the maximum speed in the time-mean eastward jet, and Rd_1 is the first baroclinic Rossby deformation radius, which is constant. Note that Re can be defined differently, by using other velocity and length scales (e.g. (Siegel et al., 2001)); our definition emphasizes the eastward jet and mesoscale eddies. In the next sections, we study how different properties of the flow depend on $Re \in [96, 10368]$, which is inversely proportional to the eddy viscosity $\nu \in [6.25, 200]\,\mathrm{m^2\,s^{-1}}$.

3.1. Numerical convergence study

This section focuses on the numerical convergence analysis and on the restrictions imposed by the eddy viscosity on the grid resolution for accurate approximation of the solution. The properly resolved flow is full of small-scale eddies concentrated around the western boundary currents and the eastward jet (Fig. 1). These eddies are responsible for the backscatter that maintains the eastward jet (Berloff, 2005), therefore, resolving them is crucial.

We identified two factors that substantially influence the quality of the solution. The first factor is statistical, and it deals with the solution spin-up and simulation times. We found that the six-year spin-up intervals (Siegel et al., 2001) do not allow the solutions to reach their statistical equilibria. Moreover, due to the interdecadal variability of the solutions (Berloff et al., 2007a; 2007b), the three-year-long records used for the analysis in (Siegel et al., 2001) can not be statistically viable. Therefore, in all our numerical experiments, the model is initially spun up from the state of rest over the required time interval $T_{\text{spin}} = \{50, 100\}$ years, which depends on the eddy viscosity ν and the number of isopycnal layers N, until the model solution becomes statistically equilibrated. Then, the solution is computed for another $T_{\text{sim}} = 100$ years and saved for analyses. As an indicator of the spin-up stages and the achieved statistical equilibria, we used the energy time series (Fig. 2). We found that less viscous flows have longer T_{spin}, and $T_{\text{spin}}^{(3)} > T_{\text{spin}}^{(6)}$ for all the solutions studied. We attribute this to the longer and stronger eastward jet extension in the 3L case and discuss this further below.

The second factor is the grid resolution needed to ensure that statistically the numerical solution is sufficiently converged to the true solution. In order to test the convergence, we computed the solution for each ν, studied in the paper, on progressively refined grids and compared the results. The grid size is assumed to be sufficient, if its halving produces only small change in the relative l^2-norm error $\delta(f,g) = \|f-g\|_2/\|g\|_2$ (Table 1), where f and g are solutions computed on the coarse and the fine grids, respectively. To study the error behaviour in the neighbourhood of the eastward jet, which is the most Re-dependent part of the solution, we introduced a similar l^2-norm error $\tilde{\delta}$ computed in the restricted domain around the jet (~20% of the basin). Note that the precursors works by Barnier et al. (1991) and Siegel et al. (2001) did not estimate the convergence of their solutions.

The largest δ were found for the most viscous solutions with $\nu = 200\,\mathrm{m^2\,s^{-1}}$ and on the 257^2 grid: $\delta(\overline{\psi}_1^{(3),129}, \overline{\psi}_1^{(3),257}) = 20\%$ and $\delta(\overline{\psi}_1^{(6),129}, \overline{\psi}_1^{(6),257}) = 15\%$. We hypothesize that these large numbers indicate the enhanced importance of marginally resolving Rd_1. In large-Re solutions, which are in the main focus of this study, δ is $1-3\%$ and $\tilde{\delta}$ is $3-4\%$ (Table 1). Relative error is not computed for the 4097^2 solutions, since the 8193^2 solution is not available, but the dependency between the required grid resolution and the eddy viscosity suggests that the 4097^2 resolution is adequate. Note that the horizontal and vertical resolutions in the largest solutions are consistent as discussed in Section 2.

To guarantee numerical convergence of the solutions, we found that the horizontal grid spacing has to be halved in each direction in response to halving ν. Note that this grid refinement halves the time step needed to maintain stable time integration. Overall, since $\overline{U}$ tends to increase with Re, on the next refined grid the computation is 10 times more expensive. It may seem that the proposed convergence criterion is too tight and leads to unnecessarily highly-accurate solutions, which do not reveal new small-scale features of the flow (especially in less viscous regimes), but in terms of the restricted error $\tilde{\delta}$, which is significantly larger than δ, the convergence criterion is not that strict.

The cumulative effect of properly resolved mesoscale eddies on the large-scale flow is illustrated by Figs. 3(a–c), where the underresolved solutions (i.e., when the large-scale flow on the coarser grid is significantly affected by the small-scale errors) on 257^2 grid are compared with the properly resolved (i.e., converged) solutions computed on 1025^2 grid. Each underresolved solution differs substantially from the converged one (Table 2): its eastward-jet penetration length L_p (i.e., the distance from the western boundary to the most eastern point at the tip of the time-mean jet, where the time-mean flow speed is less than $0.1\,\mathrm{m\,s^{-1}}$) and volume transport Q (i.e., the difference between the maximum and minimum of the time-mean barotropic transport streamfunction) are considerably smaller and the flow is less energetic. We also investigated how the grid resolution affects the eddy forcing, including its time mean $\overline{J'}$ and standard deviation $\sigma(-J')$. Comparison of 257^2 and 1025^2 solutions for $\nu = 25\,\mathrm{m^2\,s^{-1}}$ illustrates to what extent the eddy forcing is underestimated on the coarser grid (Fig. 4). The integrals of the underresolved

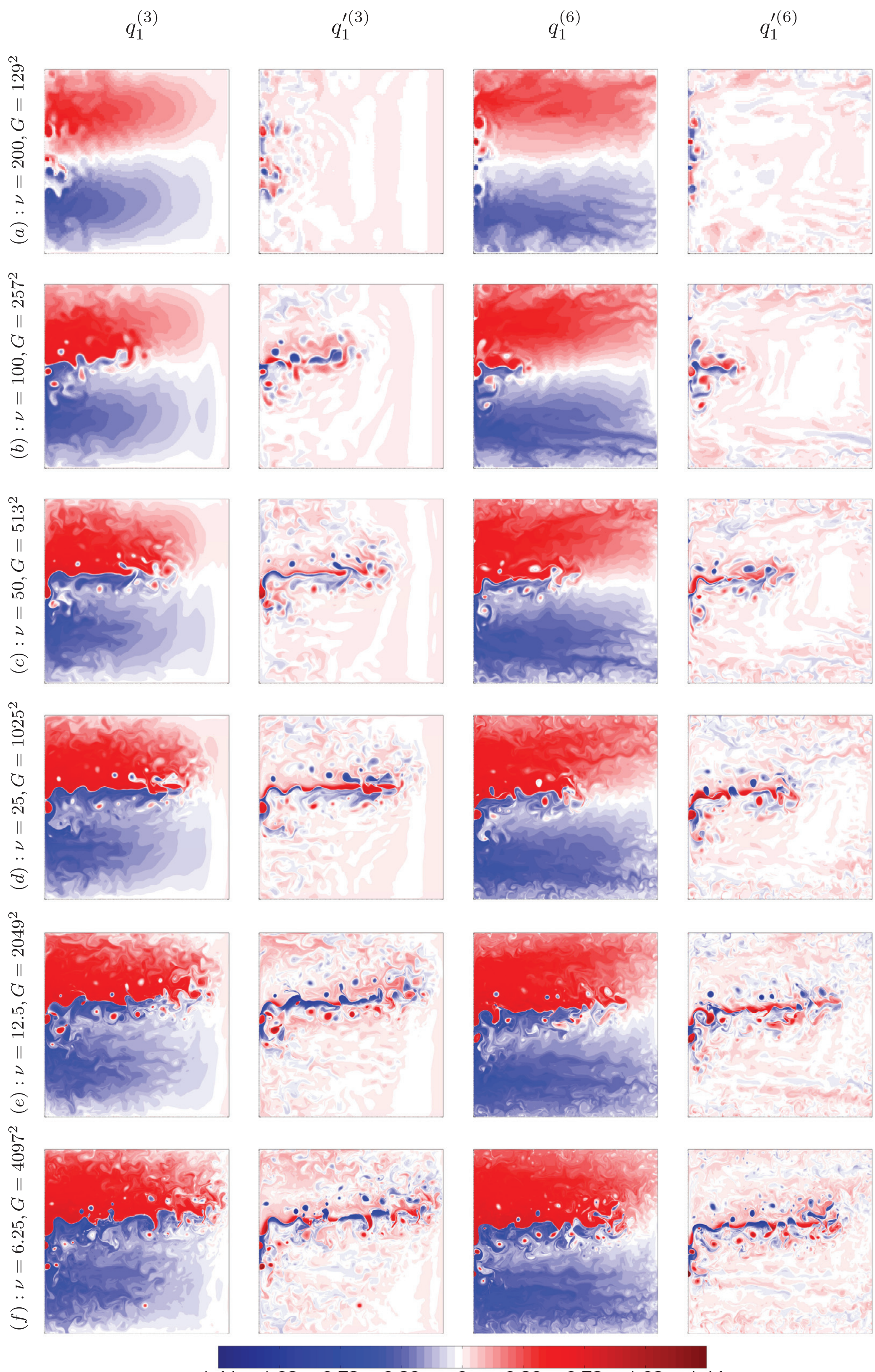

Fig. 1. A sequence of 3L and 6L solutions for increasing *Re*. Shown are an instantaneous upper-layer PV anomaly $q_1^{(3)}$ (first column) and $q_1^{\prime(3)}$ (second column), as well as $q_1^{(6)}$ (third column) and $q_1^{\prime(6)}$ (forth column), all given in units of $[s^{-1} f_0^{-1}]$, for different ν [$m^2\ s^{-1}$] and the eddy-resolving grids G; $f_0 = 0.83 \times 10^{-4}$ is the Coriolis parameter. Note that at lower ν the eddies and coherent vortices are more abundant and pronounced, and the eastward jet is always longer for the 3L solutions than for the 6L ones.

Table 1
Numerical convergence tests. The relative errors δ, $\tilde{\delta}$ and the Reynolds number Re for different eddy viscosity ν [m^2 s^{-1}] and grids G_1, G_2 on the 3L and 6L solutions; G_2 is a two times denser grid than G_1; dx [km] is the horizontal resolution. The last row is empty, because the 8193^2 solutions are not available.

G_1	dx	ν	$Re^{(3)}$	$Re^{(6)}$	$\delta(\overline{\psi}_1^{(3),G_1}, \overline{\psi}_1^{(3),G_2})$	$\tilde{\delta}(\overline{\psi}_1^{(3),G_1}, \overline{\psi}_1^{(3),G_2})$	$\delta(\overline{\psi}_1^{(6),G_1}, \overline{\psi}_1^{(6),G_2})$	$\tilde{\delta}(\overline{\psi}_1^{(6),G_1}, \overline{\psi}_1^{(6),G_2})$
129^2	29.77	200	120	96	0.20	0.55	0.15	0.46
257^2	14.94	100	444	332	0.13	0.28	0.08	0.23
513^2	7.49	50	1088	848	0.10	0.19	0.03	0.07
1025^2	3.75	25	2368	1984	0.04	0.07	0.04	0.09
2049^2	1.87	12.5	4928	4384	0.03	0.04	0.01	0.03
4097^2	0.94	6.25	10368	9472	–	–	–	–

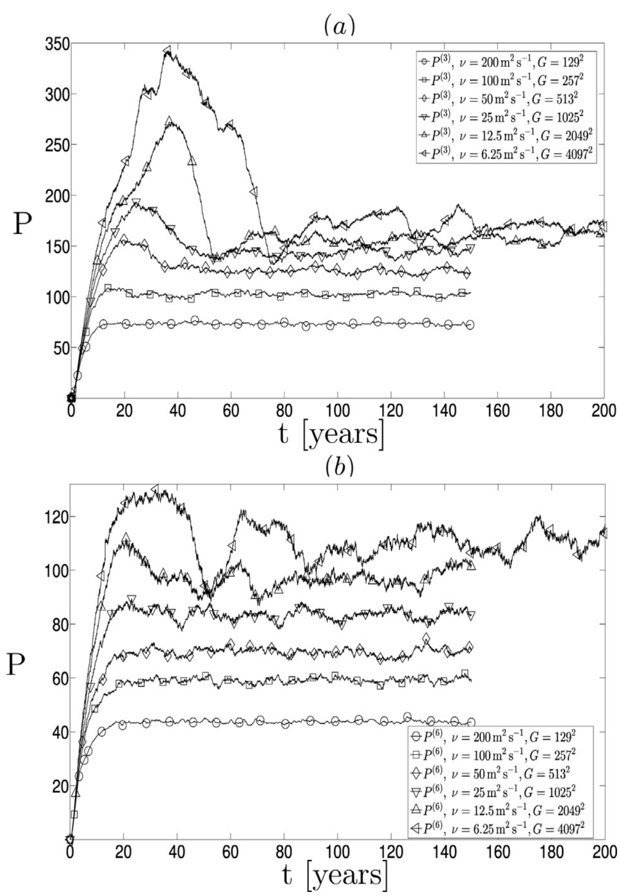

Fig. 2. Time series of the non-dimensional total potential energy P for (a) 3L and (b) 6L solutions for different values of viscosity ν. Note that low-frequency variability increases with decreasing ν. Some time series are longer than others, since the spin-up time is larger for the low-ν solutions while the simulation time is always kept equal to 100 years.

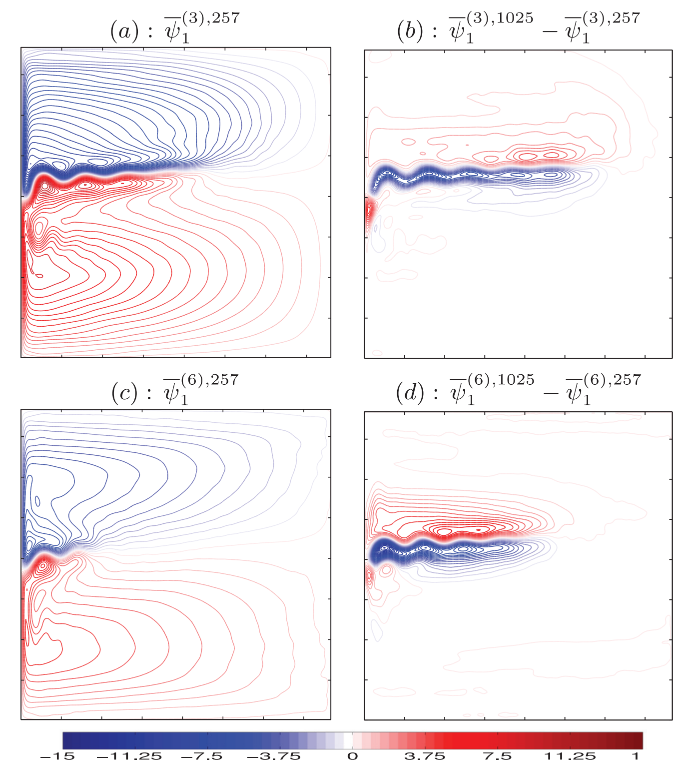

Fig. 3. Effect of the resolution error. The time-mean transport velocity streamfunction $\overline{\psi}_1$ on 257^2 and 1025^2 grids for $\nu = 25$ m^2 s^{-1}. The upper and lower panels correspond to 3L and 6L solutions, respectively; contour interval is 0.5 Sv.

Table 2
The effect due to the inadequate resolution for the eastward jet penetration length L_p, volume transport Q, the time-mean potential $\langle P\rangle$ and the eddy potential $\overline{EPE}$ energies, the time-mean upper-layer kinetic $\langle K\rangle_1$ and the eddy kinetic $\overline{EKE}_1$ energies in the 3L and 6L models for $G_1 = 257^2$, $G_2 = 1025^2$ grids, and $\nu = 25$ m^2 s^{-1}.

	3L	6L
$L_p^{G_1}/L_p^{G_2}$	0.80	0.40
Q^{G_1}/Q^{G_2}	0.84	0.66
$\langle P\rangle^{G_1}/\langle P\rangle^{G_2}$	0.83	0.70
$\overline{EPE}^{G_1}/\overline{EPE}^{G_2}$	0.83	0.70
$\langle K\rangle_1^{G_1}/\langle K\rangle_1^{G_2}$	0.72	0.56
$\overline{EKE}_1^{G_1}/\overline{EKE}_1^{G_2}$	0.41	0.34

Table 3
Resolution effects and the non-dimensional time-mean eddy forcing versus its transient part. The integral of the upper-ocean time mean eddy forcing $\overline{J}'$ and its standard deviation $\sigma(-J')$ for $\nu = 25$ m^2 s^{-1} on 257^2, 1025^2 grids for 3L and 6L solutions.

G	$I_\Omega(\lvert\overline{J'^{(3)}}\rvert)$	$I_\Omega(\lvert\overline{J'^{(6)}}\rvert)$	$I_\Omega(\sigma(-J'^{(3)}))$	$I_\Omega(\sigma(-J'^{(6)}))$
257^2	0.04×10^{-3}	0.03×10^{-3}	1.09×10^{-3}	0.75×10^{-3}
1025^2	0.06×10^{-3}	0.05×10^{-3}	1.90×10^{-3}	1.70×10^{-3}

eddy forcing $I_\Omega(|\overline{J}'|)$ and its standard deviation $I_\Omega(\sigma(-J'))$ are significantly smaller (Table 3). We hypothesize that this results in the corresponding difference between the time-mean flows (Fig. 3).

3.2. Parameter study

Sensitivity of the solutions to changes in problem parameters is an important issue that we addressed systematically. We carried out a parameter study by widely varying the main parameters of the problem: the bottom friction μ, the partial-slip parameter α and the Rossby deformation radii. Note that the radii were varied proportionally so that the ratios between them remain unchanged. Only one

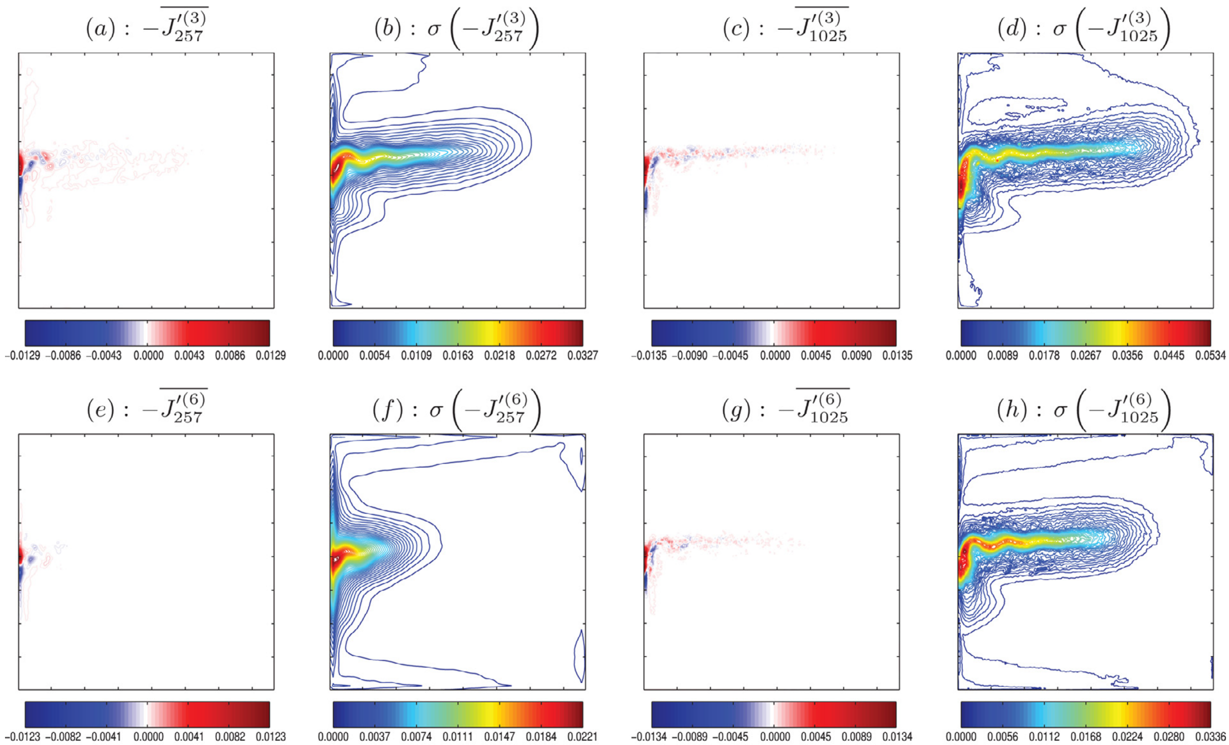

Fig. 4. Effects of the resolution error on the eddy forcing properties. The non-dimensional time mean of the fluctuating component of the upper-ocean eddy forcing $-\overline{J'}$ and its standard deviation $\sigma(-J')$ for the 3L (upper row) and 6L (lower row) solutions on 257^2 and 1025^2 grids and for $\nu = 25\,\mathrm{m^2\,s^{-1}}$. Note that except near the wester boundary, transient part of the eddy forcing completely dominates over the time-mean part.

Table 4
The effect of varying the problem parameters on the time-mean eastward jet penetration length L_p and volume transport Q in the 3L and 6L models for $\nu = 50\,\mathrm{m^2\,s^{-1}}$. The tilded function denotes the perturbed quantity as the parameter varies.

	$\widetilde{L}_p^{(3)}/L_p^{(3)}$	$\widetilde{Q}_p^{(3)}/Q_p^{(3)}$	$\delta(\widetilde{\overline{\psi}}_1^{(3)}, \overline{\psi}_1^{(3)})$	$\widetilde{L}_p^{(6)}/L_p^{(6)}$	$\widetilde{Q}_p^{(6)}/Q_p^{(6)}$	$\delta(\widetilde{\overline{\psi}}_1^{(6)}, \overline{\psi}_1^{(6)})$
$\widetilde{\mu}/\mu = 0.25$	1.05	1.12	0.09	1.12	1.13	0.10
$\widetilde{\mu}/\mu = 2.50$	0.90	0.85	0.16	0.97	0.86	0.07
$\widetilde{\alpha}/\alpha = 0.20$	0.91	0.82	0.12	0.75	0.73	0.16
$\widetilde{\alpha}/\alpha = 5.0$	1.05	1.02	0.05	1.11	1.09	0.08
$\widetilde{Rd}/Rd = 0.75$	0.56	0.77	0.79	1.01	1.14	0.19
$\widetilde{Rd}/Rd = 0.875$	0.91	1.01	0.28	1.07	1.13	0.16

parameter was varied at a time, while all the others were fixed at their main values (Section 2), and focused on main flow characteristics such as the eastward jet penetration length L_p, the volume transport Q and the relative difference δ (Table 4, Fig. 5).

In the 3L and 6L configurations, the variation of the bottom friction μ does not significantly influence the solution: $\delta(\widetilde{\overline{\psi}}_1^{(3)}, \overline{\psi}_1^{(3)}) = 15\%$ (Fig. 5a) and $\delta(\widetilde{\overline{\psi}}_1^{(6)}, \overline{\psi}_1^{(6)}) = 10\%$ (Fig. 5b), where $\widetilde{\overline{\psi}}$ is a perturbed quantity as the parameter varies. We found that the smaller/larger is μ, the larger/smaller is the difference in the 3L/6L case, and $\delta(\widetilde{\overline{\psi}}_1^{(3)}, \overline{\psi}_1^{(3)}) \approx \delta(\widetilde{\overline{\psi}}_1^{(6)}, \overline{\psi}_1^{(6)})$ for the larger μ, whereas $\delta(\widetilde{\overline{\psi}}_1^{(3)}, \overline{\psi}_1^{(3)}) > \delta(\widetilde{\overline{\psi}}_1^{(6)}, \overline{\psi}_1^{(6)})$ for the smaller μ. The eastward penetration length and the volume transport are larger and smaller in the low- and high-μ regime, respectively.

The situation is the opposite when the parameter α is varied: the smaller is α, the smaller is δ in both the 3L and 6L solutions, and $\delta(\widetilde{\overline{\psi}}_1^{(3)}, \overline{\psi}_1^{(3)}) < \delta(\widetilde{\overline{\psi}}_1^{(6)}, \overline{\psi}_1^{(6)})$ for all α considered. Note that small and large α make the partial-slip boundary condition closer to the no-slip and free-slip boundary condition, respectively.

Overall, the small α greatly reduces L_p and Q in the 3L solutions and even more so in the 6L ones (Fig. 5c), but the large α exerts a much smaller influence upon L_p and Q (Fig. 5d). For a systematic study on how α influences the western boundary current, see (Berloff and McWilliams, 1999).

The variation of the Rossby deformation radii induces more noticeable changes relative to the other parameters. In 3L solutions, $\delta(\widetilde{\overline{\psi}}_1^{(3)}, \overline{\psi}_1^{(3)}) = 79\%$, and L_p and Q are considerably smaller (Fig. 5e). However, in 6L solutions $\delta(\widetilde{\overline{\psi}}_1^{(6)}, \overline{\psi}_1^{(6)}) = 19\%$, and changes in L_p and Q do not exceed 15% (Figs. 5(e and f)). This therefore suggests that 6L solutions are less sensitive to changes in stratification, hence, more robust.

On the basis of the parameter sensitivity study, we concluded that the flow regime explored in this paper is extremely robust and characterised by the well-developed eastward jet and vigorous eddy field.

3.3. Time-mean and instantaneous flows

In this section we study how properties of the large-scale flow change with increasing Re. In particular, we look at the penetration length of the eastward jet L_p, volume transport Q, and the qualitative eddy patterns. Figs. 1 and 6 show the instantaneous and

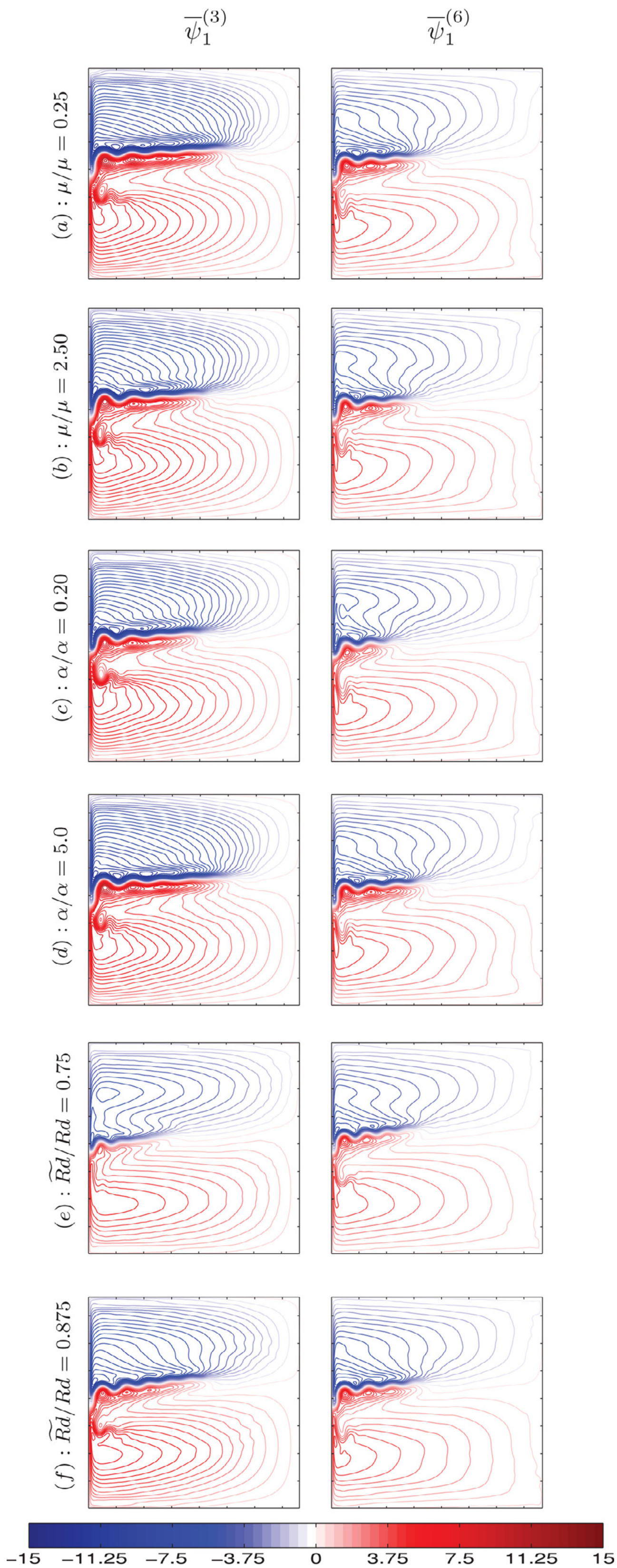

Fig. 5. The effect of varying the problem parameters (bottom friction μ, the partial-slip parameter α, and Rossby deformation radii Rd) on the time-mean transport velocity streamfunction $\overline{\psi}_1^{(3)}$ (left column) and $\overline{\psi}_1^{(6)}$ (right column) for $\nu = 50\,\mathrm{m^2\,s^{-1}}$. The tilded function denotes the perturbed quantity as the parameter varies; contour interval is 0.5 Sv.

time-mean flows for the 3L and 6L cases. All these flows have a pronounced double-gyre pattern, with the well-defined eastward jet extension generating numerous transient eddies and coherent vortices. The larger is *Re*, the stronger is the jet extension, and the richer and more intensive is the eddy field.

Our analysis is focused on the eastward jet and its adjacent recirculation zones, because this is the main eddy-driven part of the flow. The length and the volume transport of the jet echo each other: both quantities grow with *Re* and go to an asymptote in the 3L case, however, in the 6L case they tend to grow with no sign of approaching an asymptote (Fig. 7). The jet elongates at larger *Re*, and this is accompanied by the amplification of its adjacent recirculation zones. Moreover, the inequality $L_p^{(3)} > L_p^{(6)}$ holds for all *Re* studied, while $Q^{(3)} > Q^{(6)}$ is valid only for low-*Re* flows, and in large-*Re* solutions $Q^{(6)} > Q^{(3)}$ (Fig. 7). Our experiments with different basin sizes showed that $L_p^{(3)}$ and $Q^{(3)}$ approach an asymptote because of the size of the basin. On the other hand, no sign of tending to an asymptote for $L_p^{(6)}$ and $Q^{(6)}$ can be due to the large-*Re* activation of the smaller scales associated with the high baroclinic modes.

There is a remarkable difference between the 3L and 6L solutions: $L_p^{(3)}$ is significantly longer than $L_p^{(6)}$ for the whole range of *Re* (Fig. 7). This result is completely opposite to the findings of Barnier et al. (1991). This disagreement can partially be due to sufficient grid resolution in our case, but mostly it can be due to the profound difference between the explored flow regimes: Barnier et al. (1991) considered symmetric wind forcing that at large *Re* induces unrealistically strong and symmetric eastward jet. We found that high baroclinic modes in the 6L case weaken the gyres, slow down the development of the eastward jet, and $L_p^{(6)}$ and $Q^{(6)}$ do not approach an asymptote, as contrasted by comparison with 3L solutions.

The flow dependence on ν (hence, on *Re*) is shown in Fig. 1. As *Re* grows, instantaneous PV anomaly snapshots illustrate how the blurry low-*Re* flow sharpens up and becomes full of eddies and coherent vortices. We found that the characteristic vortex size is in the range of 30–140 km, and the vortex lifespan varies from about 20 days to more than three years. Being generated by the jet meanders, some vortices drift westward in the recirculation zone, where they merge with each other and ultimately become reclaimed by the jet or annihilated by the strong shear near the western boundary. These vortices are short-living. Another active vortex-formation region is located at the eastern tip of the jet. The latter vortices are more copious and also long-living, since they propagate westward along the flanks of the recirculation zones, relatively far from the jet.

In the 3L configuration, some isolated coherent vortices penetrate far into the southern gyre, as the one seen near the southern boundary (Fig. 1f). Such vortices emerge in the neighbourhood of the western boundary current separation point, propagate far upstream, and linger for years. We regard them as a 3L QG approximation artifact emerging at large *Re* due to some idealisations of the boundary-layer dynamics (e.g. flat bottom, partial-slip boundary conditions, fixed stratification). No such long-living vortices are found in the more realistic 6L solutions.

To summarize, our work studies a different from (Siegel et al., 2001) flow regime in which the eastward jet is robust and well-developed. This explains many differences between the solutions, both in the time-mean and instantaneous fields.

3.4. Flow energy

This section deals with *Re*-dependencies of the potential and kinetic energies, defined in Section 3. We found that the energies do not approach an asymptote at large *Re*. The only exception is the upper-layer mean-flow kinetic energy $\langle K\rangle_1^{(3)}$ which tends to an asymptote in the 3L case, however, the upper-layer eddy kinetic energy $\overline{EKE}_1^{(3)}$

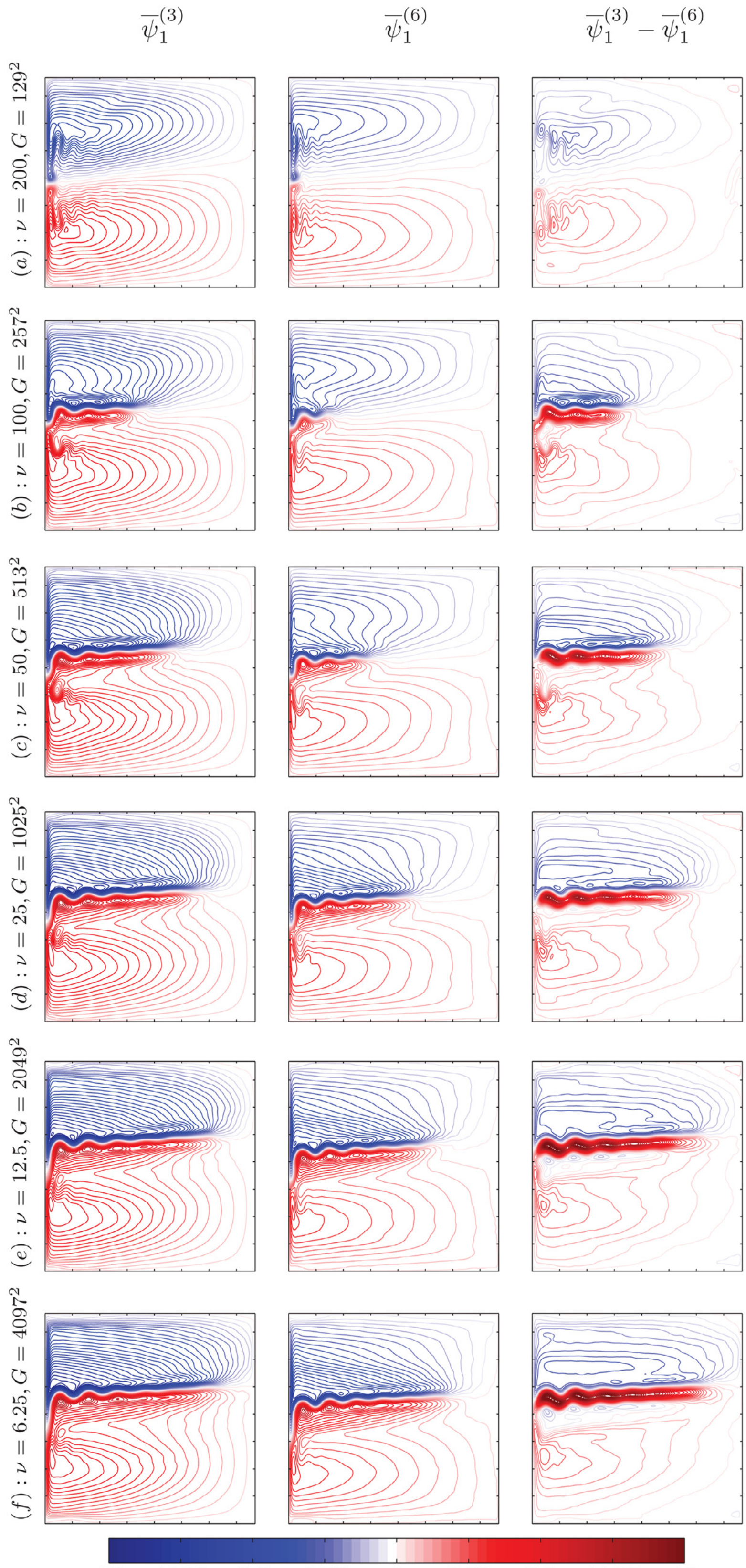

Fig. 6. A sequence of time-mean solutions for increasing *Re*. The time-mean transport velocity streamfunction $\overline{\psi}_1$: $\overline{\psi}_1^{(3)}$ (left column), $\overline{\psi}_1^{(6)}$ (middle column), and $\overline{\psi}_1^{(3)} - \overline{\psi}_1^{(6)}$ (right column) for different grids G and viscosities ν [$m^2\ s^{-1}$]; contour interval is 0.5 Sv. Note that high baroclinic modes in the 6L solutions inhibit the development of the eastward jet and reduce the strength of the gyres as opposed to the 3L solutions.

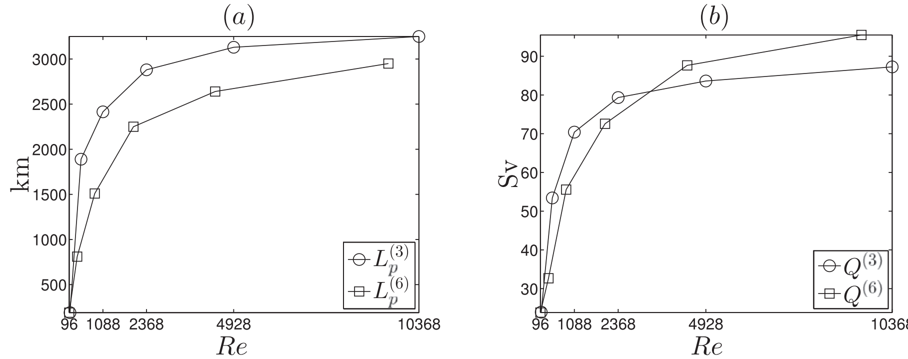

Fig. 7. The time-mean eastward jet penetration length L_p (a) and volume transport Q (b) as a function of the Reynolds number Re for 3L and 6L solutions. Note, that $L_p^{(3)}$ and $Q^{(3)}$ tend to an asymptote, whereas $L_p^{(6)}$ and $Q^{(6)}$ do not.

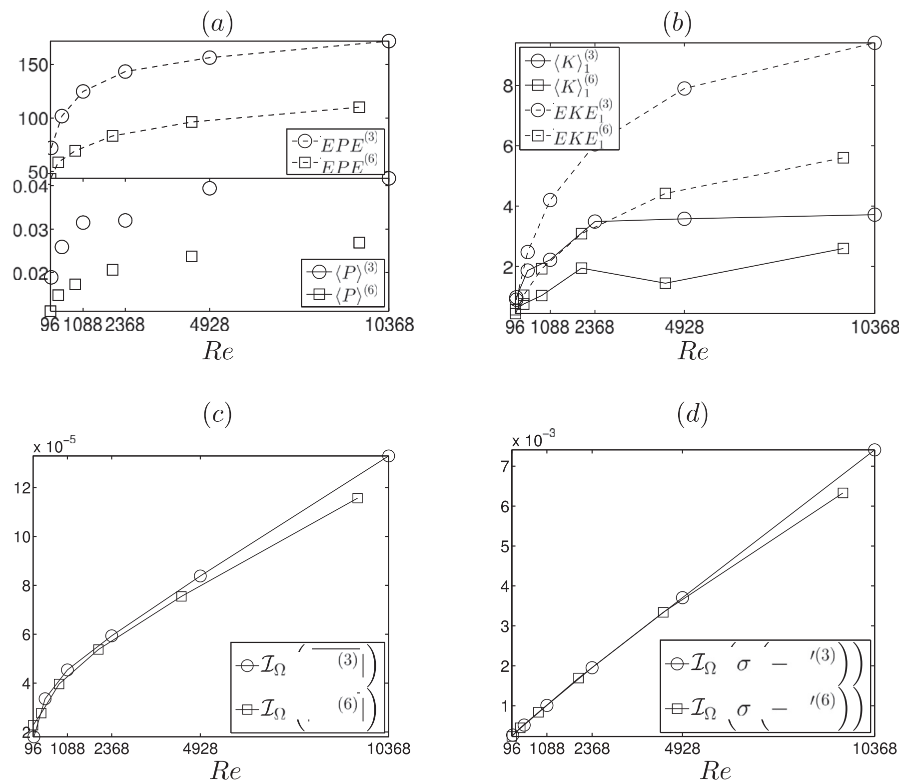

Fig. 8. Dependencies of (a) the non-dimensional mean-flow potential energy $\langle P\rangle$ and the eddy potential energy $\overline{EPE}$; (b) the upper-layer mean-flow kinetic energy $\langle K\rangle_1$ and the eddy kinetic energy $\overline{EKE}_1$; (c) the integral of the upper-ocean eddy forcing $\mathcal{I}_\Omega(|\overline{\mathcal{J}'}|)$ and (d) its standard deviation $\mathcal{I}_\Omega(\sigma(-\mathcal{J}'))$ on the Reynolds number Re for the 3L and 6L solutions.

grows rapidly with Re (Fig. 8b). In the 6L case, $\langle K\rangle_1^{(6)}$ moderately increases with Re without approaching an asymptote, while $\overline{EKE}_1^{(6)}$ rises fast akin to the 3L case. Overall, $\langle K\rangle_1^{(3)}$ and $\langle K\rangle_1^{(6)}$ increase 3.8 and 4.6 times, respectively, over the studied range of Re, while $\overline{EKE}_1^{(3)}$ and $\overline{EKE}_1^{(6)}$ rise 10.6 and 13.0 times, respectively. Note that save for the lowest-Re solution, the upper-layer eddy-kinetic energy $\overline{EKE}_1$ dominates over the mean-flow kinetic energy $\langle K\rangle_1$ and more so in the 3L configuration.

The situation with the potential energy is different. In both 3L and 6L solutions, the mean-flow potential energy $\langle P\rangle$ is three orders of magnitude smaller than the eddy potential energy $\overline{EPE}$ (Fig. 8a). The increase of $\langle P\rangle^{(3)}$ and $\langle P\rangle^{(6)}$ is much weaker, compared to $\langle K\rangle_1^{(3)}$ and $\langle K\rangle_1^{(6)}$, namely 2.2 and 2.5 times, respectively. Not much larger grow $\overline{EPE}^{(3)}$ and $\overline{EPE}^{(6)}$: 2.4 and 2.6 times, respectively. For the whole range of Re explored, $\overline{EPE}^{(3)}$ is larger than $\overline{EPE}^{(6)}$, $\langle P\rangle^{(3)} > \langle P\rangle^{(6)}$, $\langle K\rangle_1^{(6)}$ and $\overline{EKE}_1^{(6)}$ increase with Re, but remain substantially smaller than $\overline{EPE}^{(6)}$, which is dominated by the larger scales. These results do not corroborate the conclusion of (Siegel et al., 2001) that $\overline{K}_1^{(6)}$ is relatively independent on Re. Instead, we found that $\overline{K}_1^{(6)}$ is very dependable on Re (Fig. 8b). We attribute this to the above-discussed difference between the flow regimes and to the more reliable statistics in our case.

3.5. Eddy forcing and eddy PV flux

The focus of this section is on studying Re-dependencies of the eddy forcing and eddy PV flux, which are dynamically even more interesting quantities than the eddy energies, because they quantify mean flow/eddy interactions. These Re-dependencies are studied here for the first time.

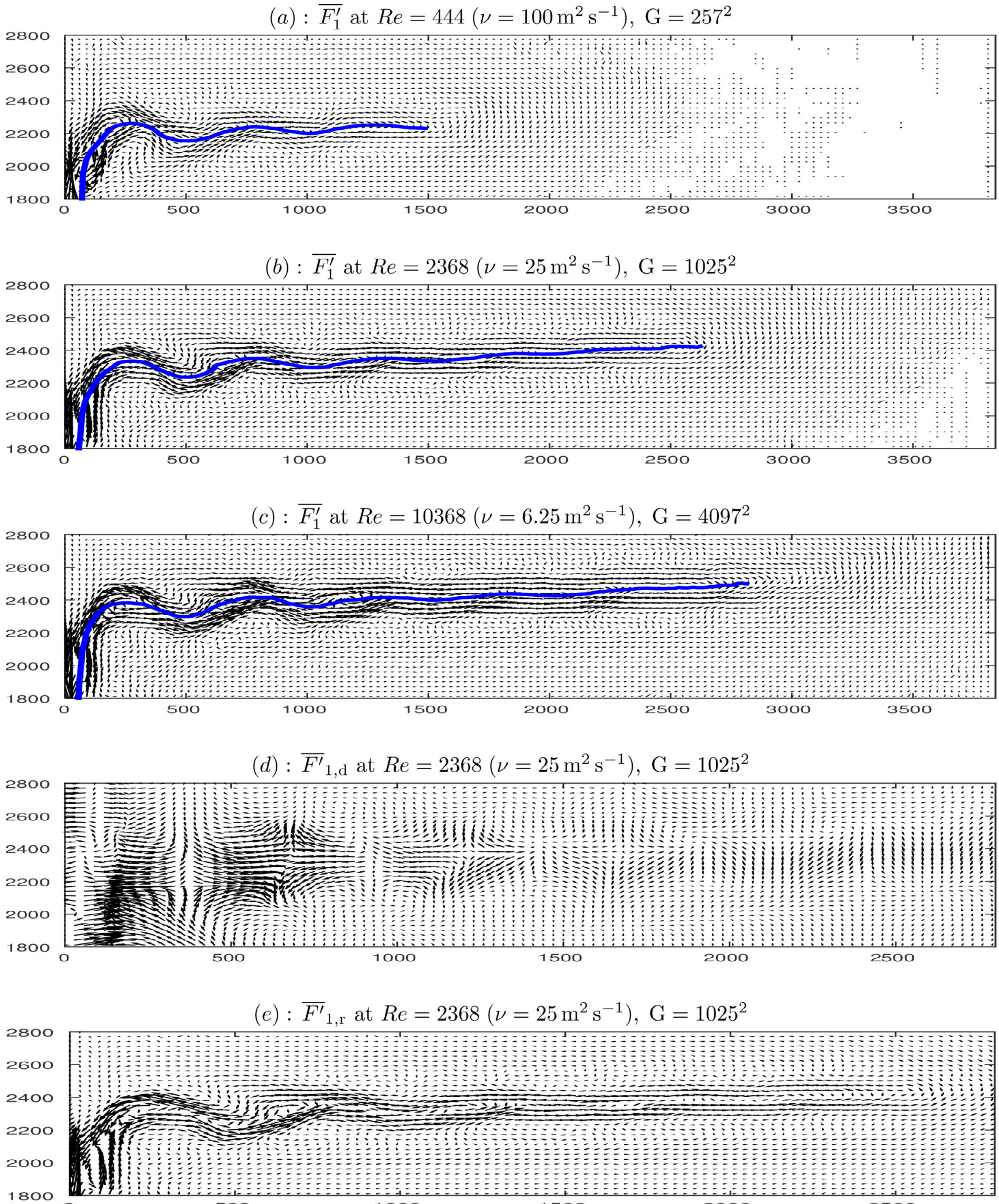

Fig. 9. Non-dimensional time-mean eddy PV flux $\overline{F_1'}$ for increasing *Re* and grids *G* in the 3L solutions; the separatrix is marked in blue. The Helmholtz decomposition of $\overline{F_1'}$ into (d) divergent $\overline{F'}_{1,\mathrm{d}}$ and (e) rotational $\overline{F'}_{1,\mathrm{r}}$ components at $Re = 2368$.

As shown in the previous section, both the eddy kinetic and potential energies increase with *Re*, and this is reflected by the basin-averaged eddy forcing $I_\Omega(|\overline{J'}|)$ and its standard deviation $I_\Omega(\sigma(-J'))$ (Figs. 8(c and d)). Both measures also do not approach an asymptote with *Re*.

We found that $I_\Omega(|\overline{J'}|)$ is by one order of magnitude smaller than $I_\Omega(\sigma(-J'))$ and the difference increases with *Re*. Thus, the transient part of the eddy forcing not only dominates over the time-mean part (Berloff, 2005; Li and von Storch, 2013), but its dominance even increases with *Re* (Figs. 8(c, d), and11(gh)).

We also studied how the upper-layer time-mean eddy PV flux $\overline{F_1'}$ depends on *Re* (Figs. 9(a,b, and c)). The flux is relatively large near the western boundary and along the eastward jet. However, its amplitude gradually attenuates as the flux transports PV from the western boundary into the interior of the basin. Using the Helmholtz decomposition we split the flux $\overline{F_1'}$ into a divergent $\overline{F'}_{1,\mathrm{d}}$ and a rotational

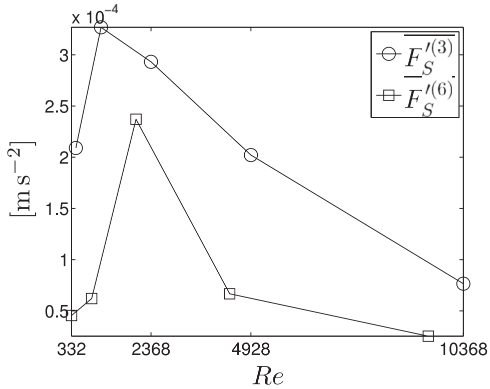

Fig. 10. Dependence of the time-mean eddy PV flux thorough the separatrix $\overline{F'_S}$ [m s^{-2}] on the Reynolds number *Re* in 3L and 6L solutions.

Table 5
Power-law dependencies of the eastward jet (EJ) characteristics on the Reynolds number *Re* for the 3L and 6L models.

EJ characteristic	Three layers	Six layers
L_p [km]	$-4\times10^4 Re^{-0.5}+4\times10^3$	$-2\times10^4 Re^{-0.04}+2\times10^4$
Q [Sv]	$-5\times10^2 Re^{-0.4}+10^2$	$-10^3 Re^{-0.02}+10^3$
$\langle K\rangle_1$	$20Re^{0.03}-20$	$0.1Re^{0.3}$
$\langle P\rangle$	$0.2Re^{0.02}-0.2$	$0.01Re^{0.1}$
$\overline{EKE}_1$	$4Re^{0.2}-10$	$0.5Re^{0.3}-2$
$\overline{EPE}$	$7\times10^2 Re^{0.03}-7\times10^2$	$50Re^{0.1}-50$
$I_\Omega(\lvert\overline{J'}\rvert)$	$10^{-6}Re^{0.4}$	$10^{-5}Re^{0.3}$
$I_\Omega(\sigma(-J'))$	$10^{-6}Re^{0.9}$	$10^{-6}Re^{0.8}$

$\overline{F'}_{1,r}$ flow component as $\overline{F'_1}=\overline{F'}_{1,d}+\overline{F'}_{1,r}$. As can be seen in Figs. 9(d and e), the divergent part of the eddy PV flux acts along rather than across the eastward jet and has no clear relation to the large-scale PV gradient.

We computed the total eddy PV flux through the separatrix $\overline{F'_S}$ (defined in Section 3) and found that this flux is always positive (Fig. 10), i.e., on average PV is transported from the southern to the northern gyre in the up-gradient sense. It is clear from Fig. 9 that divergence of the time-mean eddy flux, that is, the time-mean eddy forcing, is maintained by the diverging eddy fluxes oriented along the eastward jet and located to the north and south from its core. These fluxes correspond to the PV anomalies generated by the upstream instabilities and advected downstream along the jet. Thus, the idea of using the down-gradient PV closure

$$\overline{\mathbf{v}'q'}=-\kappa\nabla\overline{q},\quad \kappa>0$$

for the eddy parameterisation may lead to physically inconsistent flows in the vicinity of the jet.

3.6. Extrapolation of flow characteristics for larger Re

In order to study how different flow characteristics depend on very large Reynolds numbers *Re*, for which we cannot compute numerically converged solutions, we found approximate power law dependencies. To track the evolution of the flow characteristics with *Re*, we first found a power law describing the *Re*-dependence on ν ($Re^{(3)}\approx Re^{(6)}\approx 7\times10^4\nu^{-1.0}-150$) and then, given *Re*, estimated the other characteristics. Note that due to $Re^{(3)}\approx Re^{(6)}$, the Reynolds numbers for the 3L and 6L solutions have similar power laws (Table 5).

We found that in the 3L model L_p and Q approach an asymptote at large *Re* and their values go to $L_p^{(3)}=3520$ km and $Q^{(3)}=95$ Sv (Figs. 11(a and b)). This is due to the finite size of the basin limiting the jet. However, in the 6L case these quantities do not tend to an asymptote. This can be due to activation of smaller scales associated with the high baroclinic modes or due to the jet length being shorter and less affected by the basin size.

The mean-flow potential energies $\langle P\rangle^{(3)}$ and $\langle P\rangle^{(6)}$ demonstrate a very moderate increase with *Re* (Fig. 11c), whereas the eddy potential energies $\overline{EPE}^{(3)}$ and $\overline{EPE}^{(6)}$ grow rapidly (Fig. 11d). Due to the intensifying energy transfer from the large to small scales, $\langle K\rangle_1^{(3)}$ and $\langle K\rangle_1^{(6)}$, as well as $\overline{EKE}_1^{(3)}$ and $\overline{EKE}_1^{(6)}$, robustly increase with *Re* (Figs. 11(e and f), but remain smaller than $\overline{EPE}^{(3)}$ and $\overline{EPE}^{(6)}$, which are dominated by the large-scale flow. The potential and kinetic 6L energies are smaller than the 3L ones, but their increase rates are higher (see Section 3.4). The eddy kinetic energy increases faster than the mean-flow energy, and as we found, this increase is associated with increasing eddy forcing (Fig. 11g).

We found that high baroclinic modes in 6L solutions slow down the development of the eastward jet, weaken the gyres, and preclude an asymptote for $L_p^{(6)}$ and $Q^{(6)}$, as contrasted by comparison with 3L solutions. Besides, $L_p^{(3)}>L_p^{(6)}$ for all *Re* studied, whereas $Q^{(3)}>Q_p^{(6)}$ in low-*Re* regimes and $Q^{(3)}<Q_p^{(6)}$ for high-*Re* solutions (Fig. 7). The latter is due to the more intense deep-ocean circulation in the large-*Re* 6*L* solution.

4. Conclusions and discussion

The purpose of this research is to analyse how different aspects of turbulent geostrophic flows, such as time-mean linear and quadratic properties, as well as instantaneous flow features depend on the Reynolds number *Re*. The motivation of the study is twofold: to understand the evolution of eddy/mean flow interactions as more and more degrees of freedom become dynamically available at progressively larger Reynolds numbers, and to establish a set of benchmark double-gyre solutions and put forward a methodology for systematic analyses of *Re*-dependencies. We propose to adopt this methodology for analyses of comprehensive general circulation models (GCMs).

We studied the classical quasi-geostrophic double-gyre model in the idealised closed-basin configuration, with both three and six isopycnal layers (3L and 6L models), for a broad range of Reynolds numbers $Re\in[96, 10368]$ achieved by varying the eddy viscosity ν in the range from 200 m^{2}s^{-1} to 6.25 m^{2}s^{-1}, and for long 100 year simulations, all carried out on the computational grids ranging from 129^2 to 4097^2 points. Despite the use of powerful supercomputers and efficient numerical methods, we could not exercise horizontal grid resolutions larger than 4097^2 and penetrate the curtain of even larger *Re*. Moreover, increasing the number of vertical layers is also problematic, since using more than six layers will inevitably require denser horizontal grids to keep the vertical and horizontal resolutions consistent with solution convergence, as smaller length scales corresponding to the new deformation radii become available.

The primary criterion we were guided by in choosing the quasi-geostrophic model for study was the following: first, this is a classical oceanic model which simulates the mesoscale motions far beyond its formal limits of applicability, e.g. (Mundt et al., 1997; Zurita-Gotor and Vallis, 2009); second, the relative simplicity of the model allows for its systematic exploration in eddy-resolving regimes, which is beyond reach of OGCMs; and third, this model offers a wide palette of dynamically viable and featurely enriched oceanic flows available for exploration. For the sake of fairness, it is worth noting that although the QG model allows us to study various flow regimes it filters out gravity waves and other unbalanced motions, which, however, can be handled with OGCMs but in relatively small domains and on short simulation times.

The configuration of the model was chosen so that it enables one to work in eddy-resolving regimes and, most importantly, with converged solutions. We also adapted our parameters, as close as possible, to those used by our precursors (Barnier et al. (1991) and

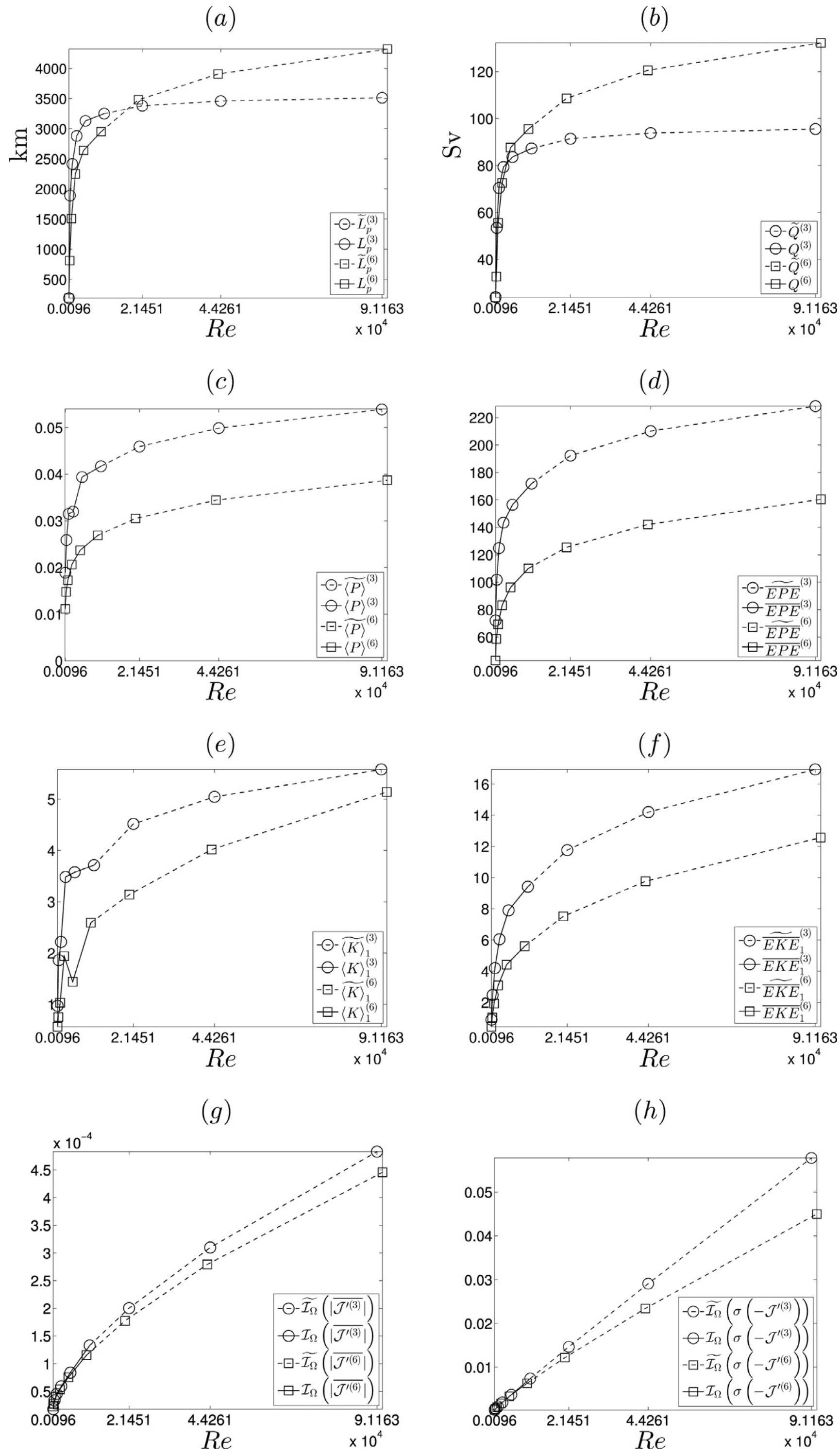

Fig. 11. Dependencies of different extrapolated flow characteristics in the 3L and 6L configurations on the Reynolds number *Re*; the tilded functions indicate extrapolated quantities. Shown are (a) the penetration length L_p [km], (b) the volume transport Q [Sv], (c) the non-dimensional mean-flow potential energy $\langle P\rangle$, (d) the non-dimensional eddy potential energy $\overline{EPE}$, (e) the non-dimensional mean-flow upper-ocean kinetic energy $\langle K\rangle_1$, (f) the non-dimensional upper-ocean eddy kinetic energy $\overline{EKE}_1$, (g) the integral of the eddy forcing $I_\Omega(\overline{|J'|})$ and (h) its standard deviation $I_\Omega(\sigma(-J'))$.

Siegel et al. (2001)), but also in a such way that our solutions operate in the robust flow regime characterised by the well-developed and coherent eastward jet extension of the western boundary currents, such as the Gulf stream and Kuroshio. The parameter study showed that both the 3L and 6L solutions are quite insensitive to changes in the governing parameters. Moreover, the 6L solutions demonstrate even less receptivity to the parameters alterations. The difference between our model and the ones used by Barnier et al. (1991) and Siegel et al. (2001) lies in the wind stress amplitude (which is about two times smaller in our case), the boundary conditions (we use the partial-slip condition instead of the no-slip in (Siegel et al., 2001) and free-slip in (Barnier et al., 1991), the horizontal resolution (360 × 320 in (Barnier et al., 1991) and 2048^2 in Siegel et al. (2001) against 4097^2 in our model), and both the spin up and simulation times ($T_{spin} = 6$ years and $T_{sim} = 7$ years in (Barnier et al., 1991); $T_{spin} = 3$ years and $T_{sim} = 6$ years in Siegel et al. (2001) compared with $T_{spin} = 100$ years and $T_{sim} = 100$ years used in our simulations). All these factors make the jet underdeveloped in Siegel et al. (2001) and overdeveloped in Barnier et al. (1991).

Our study continues and extends the earlier works by Barnier et al. (1991) and Siegel et al. (2001), and some of our findings and conclusions are different from the earlier ones. Let us review the novel aspects of our work. First, we conducted a thorough numerical convergence study and found the solutions converged on the proper grids. Second, we considerably increased the spatial resolution of the model, spin-up and simulation times to obtain more physically reliable flows and more accurate statistics. All this increased our computational costs by a factor of about 8500 and 550, in terms of the degrees of freedom and simulation time, compared to the works (Barnier et al., 1991) and (Siegel et al., 2001), respectively. Third, we studied the model solutions for both a much broader range and much larger values of *Re*, and thus reached dynamically more realistic flow regimes characterised by the robust eastward jet extension of the western boundary currents. Forth, we not only analysed the kinetic energy, as in (Siegel et al., 2001), but also the potential energy, the time mean and standard deviation of the eddy forcing as well as the penetration length and volume transport of the eastward jet. Instead of studying a longitudinal average of the eddy PV flux, as in (Siegel et al., 2001), we investigated the full eddy PV flux and computed its value through the separatrix between the gyres. Fifth, we studied the effect of the high baroclinic modes and came to the opposite to earlier work (Barnier et al., 1991) conclusions. Sixth, we obtained empirical power laws for the potential and kinetic energies, the jet penetration length and volume transport to study the behaviour of these flow properties for larger *Re*.

Our main findings about the flow dependencies on *Re* are the following. First, the main feature of the *Re*-dependence is a progressive amplification of the eastward jet and its adjacent recirculation zones, all maintained by the eddy backscatter mechanism (e.g. Berloff (2005)). Second, from the solution convergence study, we found that halving the eddy viscosity ν requires approximately halving the grid spacing, in order to keep the large-scale effects of the small-scale numerical errors relatively small. By these standards a GCM with a resolution of $1/12^\circ$ permits ν not less than $50\,\mathrm{m}^2\,\mathrm{s}^{-1}$. Third, the parameter study suggests that the 6L-solutions are less influenced by changes in the governing parameters (the bottom friction μ, the partial-slip parameter α in the boundary condition (4) and the Rossby deformation radii) than the 3L ones. Fourth, from the empirical power laws we concluded that at large *Re* the time-mean flow properties, such as the jet penetration length and volume transport tend to an asymptote and grow in the 3L and 6L models, respectively. However, the time-mean flow energy and eddy energy as well as the time-mean kinetic energy do not approach an asymptote at large *Re* as opposed to (Siegel et al., 2001). The basin-averaged time-mean eddy forcing $I_\Omega\left(|\overline{J'}|\right)$ and its standard deviation $I_\Omega\left(\sigma\left(-J'\right)\right)$ also increase with *Re* and exhibit no tendency to approach an asymptote. Moreover, $I_\Omega\left(\sigma\left(-J'\right)\right)$ is by one order of magnitude larger than $I_\Omega\left(|\overline{J'}|\right)$, and this difference grows with *Re*. Amplification of the eddy forcing fluctuations is consistent with stronger eddy backscatter that maintains the eastward jet and its adjacent recirculation zones (Berloff, 2005). Fifth, our findings suggest that the down-gradient PV closure can result in physically inconsistent flows, since PV is transported from the southern gyre to the northern one in the up-gradient sense. Sixth, the vortex generation is mostly performed by meanders of the eastward jet and around its eastern extremity. The former process was noted in (Siegel et al., 2001), but here we found that the latter process dominates, because it spawns coherent vortices living longer and travelling over larger distances. Seventh, the effect of the high baroclinic modes significantly reduces the length of the eastward jet and the strength of the gyres, thus making an inhibitory rather than a catalytic impact on the flow, unlike previously thought (Barnier et al., 1991). This contradiction with the previous work is explained by the combination of its insufficient grid resolution with the choice of artificially symmetric wind stress, that maintains unrealistically strong and long eastward jet, not present in our solutions.

Summarising the main reasons for the differences between our study and the one by Siegel et al. (2001) we contend that they come from the following: the six year spin-up intervals in (Siegel et al., 2001) are too short to reach the statistical equilibrium; the three year solutions used for the analysis in (Siegel et al., 2001) are too short to average over the intrinsic interdecadal variability and, therefore, they contain statistical biases; the large-*Re* solutions in (Siegel et al., 2001) do not have the coherent eastward jet extension due to the no-slip boundary condition even with the wind stress amplitude two times higher than ours, and, thus, operate in a less realistic regime.

Our results suggest the following future research avenues. First, our approach to understanding Reynolds number effects can be applied to primitive-equation GCMs in both idealised and realistic configurations, with the goal to understand dependencies of the eddies and their large-scale effects on *Re*. Second, we demonstrated that the eddy parameterisations should take into account the eddy backscatter mechanism and the resulting amplification of the eastward jet extension of the western boundary currents and its adjacent recirculation zones; development of such parameterisations may require completely new approaches. Third, our study left completely aside theoretical and practical questions about the passive-tracer transport and stirring induced by the eddies (e.g. estimates of the corresponding inhomogeneous and anisotropic eddy diffusivities).

Acknowledgements

The authors are thankful to the Natural Environment Research Council for the support of this work through the grant NE/J006602/1 and the use of ARCHER (the UK National Supercomputing Service). We express our gratitude to Simon Burbidge and Matt Harvey for their help with Imperial College London cluster. The authors would also like to thank unknown referees for valuable comments and suggestions, which helped us to improve the paper.

References

Armstrong, E., Chin, T., Vazquez, J., Menemenlis, D., 2014. Sea surface temperature characterization using a high-resolution ocean model. Proceedings of the GHRSST XV science team meeting. 140.
Barnier, B., Provost, C.L., Hua, B.L., 1991. On the catalytic role of high Baroclinic modes in eddy-driven large-scale circulations. J. Phys. Oceanogr. 21 (7), 976–997.
Berloff, P., 2005. On dynamically consistent eddy fluxes. Dynam. Atmos. Ocean. 38 (3–4), 123–146.
Berloff, P., Dewar, W., Kravtsov, S., McWilliams, J., 2007a. Ocean eddy dynamics in a coupled ocean-atmosphere model. J. Phys. Oceanogr. 37 (5), 1103–1121.
Berloff, P., Hogg, A., Dewar, W., 2007b. The turbulent oscillator: a mechanism of low-frequency variability of the wind-driven ocean gyres. J. Phys. Oceanogr. 37 (9), 2363–2386.
Berloff, P., McWilliams, J., 1999. Quasigeostrophic dynamics of the western boundary current. J. Phys. Oceanogr. 29 (10), 2607–2634.
Gula, J., Molemaker, M.J., McWilliams., J.C., 2015. Gulf stream dynamics along the southeastern U.S. seaboard. J. Phys. Oceanogr. 45 (3), 690–715.
Holland, W.R., 1978. The role of mesoscale eddies in the general circulation of the ocean-numerical experiments using a wind-driven quasi-geostrophic model. J. Phys. Oceanogr. 8 (3), 363–392.
Karabasov, S.A., Berloff, P.S., Goloviznin, V.M., 2009. CABARET in the ocean gyres. Ocean Modell. 30 (2-3), 155–168.
Li, H., von Storch, J.-S., 2013. On the fluctuating buoyancy fluxes simulated in a OGCM. J. Phys. Oceanogr. 43, 1270–1287.
Marsh, R., A. de Cuevas, B., Coward, A.C., Jacquin, J., Hirschi, J.J.-M., Aksenov, Y., Nurser, A.J.G., Josey, S.A., 2009. Recent changes in the North Atlantic circulation simulated with eddy-permitting and eddy-resolving ocean models. Ocean Modell. 28 (4), 226–239.
McWilliams, J.C., 1977. A note on a consistent quasigeostrophic model in a multiply connected domain. Dynam. Atmos. Ocean. 1 (5), 427–441.

Mundt, M.D., Vallis, G.K., Wang, J., 1997. Balanced models and dynamics for the large- and mesoscale circulation. J. Phys. Oceanogr. 27 (6), 1133–1152.
Pedlosky, J., 1987. Geophysical Fluid Dynamics. Springer-Verlag, New York.
Roullet, G., McWilliams, J., Capet, X., Molemaker, M., 2012. Properties of steady geostrophic turbulence with isopycnal outcropping. J. Phys. Oceanogr. 42 (1), 18–38.
Siegel, A., Weiss, J.B., Toomre, J., McWilliams, J.C., Berloff, P.S., Yavneh, I., 2001. Eddies and vortices in ocean basin dynamics. Geophys. Res. Lett. 28 (16), 3183–3186.
Treguier, A.M., Deshayes, J., Le Sommer, J., Lique, C., Madec, G., Penduff, T., Molines, J.-M., Barnier, B., Bourdalle-Badie, R., Talandier, C., 2014. Meridional transport of salt in the global ocean from an eddy-resolving model. Ocean Sci. 10, 243–255.
Vallis, G.K., 2006. Atmospheric and Oceanic Fluid Dynamics: Fundamentals and Large-scale Circulation. Cambridge University Press, Cambridge, UK.
Zurita-Gotor, P., Vallis, G.K., 2009. Equilibration of baroclinic turbulence in primitive equations and Quasigeostrophic Models. J. Atmos. Sci. 66 (4), 837–863.